Anionic Stacks of Alkali-Interlinked Yttrium and Dysprosium Bicyclooctatetraenes in Isolation

Erik K. Schneider, Patrick Weis, Luca Münzfeld, Peter W. Roesky, and Manfred M. Kappes*

ABSTRACT: Electrospray ionization of THF solutions of preformed $[K(18\text{-c-}6)][M(COT)_2]$ (M = Dy(III), Y(III); COT = $C_8H_8^{2-}$,18-c-6 = $C_{12}H_{24}O_6$) yields the isolated species $[(M(COT)_2)_{n+1} + nK]^-$ with n = 0−3. High-resolution ion mobility spectrometry combined with density functional theory calculations performed for the n = 0−2 aggregates indicate that anionic multidecker stacks interlinked by potassium cations are formed. The alternating metal ions are aligned linearly: COT^{2-}−M^{3+}−COT^{2-}−K^+−COT^{2-}−M^{3+}−COT^{2-}. The different M^{3+} ionic radii lead to slight but resolvable changes in mobility and thus collision cross sections indicative of different overall heights of the multidecker stacks. CID measurements show that the aggregates fragment by cleavage at the K^+ interconnections.

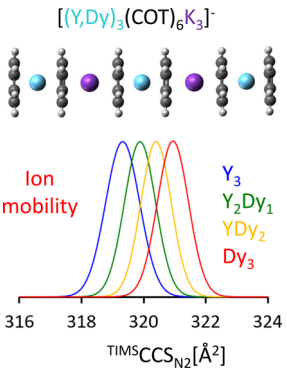

INTRODUCTION

Single- and double-decker sandwich complexes of lanthanide atoms with cyclooctatetraenyl (COT = C_8H_8) ligands were first accessed synthetically more than 40 years ago.[1,2] However, exploration of the interesting physical properties of these materials has been hindered by their extreme air and moisture sensitivity.

A completely different approach to make and study these and related double- and also multidecker stacks was found ca. 25 years ago. It involves laser vaporization of metal atoms in a gaseous stream of the ligands of interest to form collimated molecular beams which can be probed with mass spectrometric methods. Overall, this approach generates much less material than in condensed-phase synthesis, but the species entrained in the molecular beams are fully *isolated* (and thus protected) from their environment. In this way, first vanadium benzene multideckers were demonstrated and their linear stacking motif inferred by low-resolution ion mobility spectrometry.[3,4] Shortly thereafter, molecular beams of $Ln_n(COT)_{n+1}$ species (neutral and ionic, Ln = lanthanide) were analogously generated. Collision-induced dissociation (CID), photoionization mass spectrometry, and photoelectron spectroscopy (PES) were used to infer that the corresponding aggregates comprised a linear multidecker sandwich structure with up to 30 Ln(III) or Ln(II) centers individually intercalated between COT rings.[5,6] Stern−Gerlach deflection of neutral $(Ln)_n(COT)_{n+1}$ aggregates indicated weak antiferromagnetic coupling of Tb(III) or Ho(III) spin centers separated by nominally planar COT^{2-} moieties.[7] This inference of through-COT^{2-} coupling was more recently supported by the STM-based observation of ferromagnetic nanowire stacks of Eu(COT) comprising more than 1000 units, grown on graphene substrates by codepositing Eu and COT.[8]

The molecular beam method (laser vaporization of lanthanide metal rods in a stream of COT vapor) has allowed detailed PES studies of $[Ln(COT)_2]^-$ as a function of Ln.[9] Apart from dramatic differences across the lanthanide series observed in particular for Eu and Yb (interpreted in terms of different element-specific oxidation states), these measurements resolved moderate PES pattern variations between light/heavy Ln on the one side and mid-Ln elements on the other.[5,9,10] These results have stimulated extensive recent quantum chemical calculations focusing on the Ln-element specific description of spin−orbit coupling in Ln(III) vs Ln(II).[11]

The pioneering studies of the properties of isolated $[Ln(COT)_2]^-$ and $(Ln)_n(COT)_{n+1}$ have inspired us to explore a different approach toward obtaining isolated anionic aggregates of preformed double-decker rare earth dysprosium and yttrium complexes. The dysprosium complex was synthesized due to its unusual magnetic properties (high spin) and the yttrium compound for comparison since it has similar chemistry but is diamagnetic.[12] Here, we show that it is possible to generate linear, alkali-cation-interlinked stacks of up to four $[M(COT)_2]^-$ units by electrospray ionization of THF

solutions of the as-prepared $[M(COT)_2]^-$ complexes stabilized by $[K(18\text{-c-}6)]^+$ counterions counterions.

We use high resolution ion mobility spectrometry (IMS), DFT calculations and trajectory method calculations to study these aggregates and to prove that they form linear multidecker stacks with slight but measurable M-dependent variations in height. Furthermore, we have used energy resolved CID measurements (in combination with DFT) to explore the corresponding fragmentation energetics.

METHODS

Preparation of [K(18-c-6)][M(COT)$_2$] (M = Y, Dy). The synthesis was performed following the modified literature procedures.[12−14]

The starting material $[K_2COT]$ was prepared in situ by slowly adding cyclooctatetraene (1.00 equiv, 3.58 mmol, 373 mg) to a vigorously stirred suspension of finely cut potassium (2.50 equiv, 8.95 mmol, 350 mg) in THF (15 mL) at −78 °C. Subsequently, the reaction mixture was allowed to warm to room temperature and stirred for 12 h. The resulting suspension was directly filtered over a medium porosity sintered glass frit onto a slurry of the corresponding MCl_3 (0.50 equiv, 1.79 mmol, 350 mg for Y and 480 mg for Dy) in THF (20 mL) and stirred for 12 h at room temperature. Afterward, the reaction mixture was extracted with hot THF until the extracts remained colorless. To these extracts was added a solution of 18-crown-6 (18-c-6:0.50 equiv, 1.79 mmol, 451 mg) in 10 mL of THF and the resulting solution stirred at room temperature for 1 h. Afterward, the solvent was removed in vacuo until crystallization was observable. The obtained microcrystalline material was stored at −30 °C for 2 days to induce further crystallization. The desired compounds were then isolated by decantation of the mother liquor and drying in vacuo. Yield: 462 mg for Y (43%) and 772 mg for Dy (64%).

All manipulations of air-sensitive materials (including filling of syringes for transfer to the electrospray source of the mass spectrometer) were performed under rigorous exclusion of oxygen and moisture in flame-dried Schlenk-type glassware either on a dual manifold Schlenk line, interfaced to a high vacuum (10^{-3} Torr) pump, or in an argon-filled MBraun glovebox. Tetrahydrofuran (THF) was predried using an MBraun solvent purification system (SPS-800) and additionally distilled under nitrogen over potassium before storage in vacuo over $LiAlH_4$. THF-d_8 was dried over Na/K alloy and directly distilled into NMR samples. Cyclooctatetraene was stored over molecular sieves 3 Å and freshly distilled before usage.

The Supporting Information (Figure S1−S3) contains ^{1}H NMR and ^{13}C(^{1}H) NMR of the products in THF-d_8 to document purity levels.

ESI-MS, CID, and IMS Measurements. A Bruker ESI-timsTOF instrument was used to obtain high-resolution electrospray mass spectra (MS, $m/\Delta m$ > 23000) for energy-resolved collision induced dissociation (CID) measurements and for mass-selective trapped ion mobility spectrometry (TIMS) in N_2 collision gas. The operating principle of TIMS, a recently introduced high resolution variant of ion mobility spectrometry, is described in ref 15. TIMS measurements are carried out using a so-called "TIMS-tunnel" in which electrostatically trapped ions are sorted in space according to their differing mobilities and then sequentially released into a mass spectrometer detector by ramping the trapping potential. In this study, the TIMS tunnel was operated at the highest feasible ion mobility resolution by maximizing ramp time (500 ms) while keeping the mobility scan range as small as possible (0.1 Vs/cm^2). Experimental ion mobilities were converted into collision cross sections ($^{TIMS}CCS_{N2}$) using the Mason−Schamp equation.[16] Agilent TuneMix was used for $^{TIMS}CCS_{N2}$ calibration.[17] In this study, calibrated $^{TIMS}CCS_{N2}$ values were typically obtained at a resolution (CCS/ΔCCS > 120). This is less than we have achieved in some of our other published TIMS studies (CCS/ΔCCS ≈ 200)[18,19] because of the comparatively low accessible ESI ion signals (which in turn required long accumulation times).

Typical ESI source conditions (negative ion mode) were as follows: spray voltage 3 kV, drying-gas flow 3.5 L/min, analyte syringe pump speed 3 μL/min. We used solutions of 0.8 mmol/L and capillary temperatures of 200 °C.

In the timsTOF instrument, variable energy CID measurements are carried out using a linear quadrupole ion guide collision cell (containing molecular nitrogen collision gas) mounted between a quadrupole mass filter for mass selection and a reflectron time-of-flight mass spectrometer for analysis of charged fragments. For CID measurements, the TIMS tunnel which is situated upstream from the quadrupole mass filter was used in transmission mode. Relative precursor ion intensities, SY (Survival Yield), obtained from fragment mass spectra according to eq 1 were used to generate breakdown curves by plotting SY versus acceleration voltage (= lab frame collision energy).

$$SY = \frac{I_{precursor}}{I_{precursor} + \sum_i I_{fragment,i}} \quad (1)$$

Turning point energies, ECE_{50}, of the corresponding breakdown curves were determined by fitting a function of the form

$$SY(E) = \frac{1}{1 + \exp\left(\frac{E - ECE_{50}}{a}\right)} \quad (2)$$

where a corresponds to the slope at the turning point.

Theory. Quantum chemical calculations were carried out at the DFT level of theory using the Turbomole[20] program package with the functional TPSS,[21−23] and the basis set def2-SVP[24−28] as well as the RI-approximation[24,26,29,30] and dispersion correction D3.[31] The TPSS functional has been shown to perform reasonably well for lanthanide containing molecules.[32] All geometries were fully optimized without any symmetry restrictions. While the pure yttrium-containing species are closed shell systems, replacing Y(III) with Dy(III) leads to open-shell systems. We chose the high spin state with five unpaired electrons per Dy(III) in all calculations. This is the preferred spin state for dysprosium, since for 4f-electrons spin-pairing energy usually exceeds the ligand-field stabilization.[33] Furthermore, test calculations showed that the sextet state is lowest, the quartet is 1.00 eV and the doublet 2.87 eV higher in energy.

Trajectory method (TM) calculations (of N_2 scattering from the ions[36,37]) were used to compare structural models derived from DFT calculations with calibrated $^{TIMS}CCS_{N2}$ values from experiment. For this we used the IMoS 1.09 program package.[34,35] We include in the TM calculations both ion-induced dipole interactions and ion-quadrupole interactions (option qpol = 1 in IMoS). For this we use the partial charges based on the Mulliken population analysis, Merz−Kollman−

Singh (MKS)[36] and Natural Population Analysis (NPA).[37] Further details are described in the Results below.

RESULTS

ESI-MS. We sprayed both pure and mixed solutions of [K(18-c-6)][M(COT)$_2$], M = Y, Dy in THF. The anion mass spectra of the pure substances show M(COT)$_2^-$ and [(M(COT)$_2$)$_{n+1}$+ nK]$^-$ clusters with n = 1−3. Their relative intensities depend somewhat on spray conditions and solution concentrations but drop off roughly exponentially with increasing monomer count. Figure 1 shows overview mass

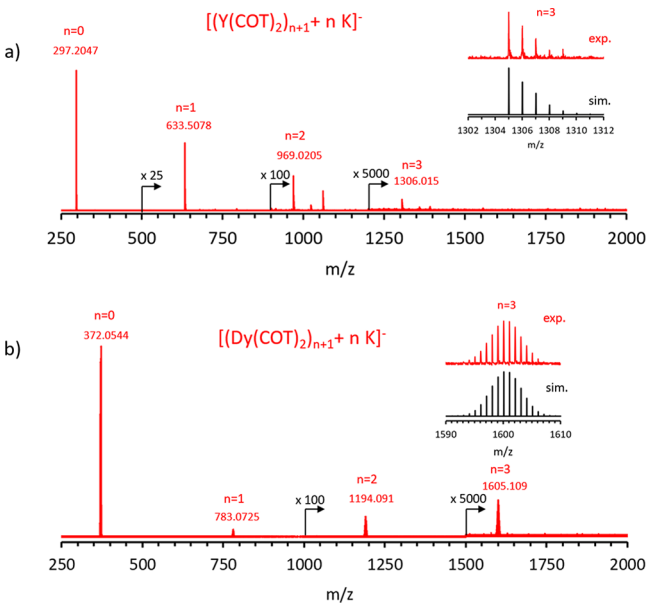

Figure 1. Overview anion mass spectra. Shown in the insets is an expanded scale view of the respective tetramer anion (n = 3; [(M(COT)$_2$)$_4$ + 3 K] ; M = Dy, Y), with resolved isotope pattern (exp) and corresponding simulation (sim).

spectra together with an expanded scale insert of the tetramer (n = 3) region highlighting the measured isotope pattern and its quantitative simulation. Gas-phase complexes of M(COT)$_2^-$ with crown ethers were not observed. We note in passing, that analogues of the n = 2 dimer species observed here in gas-phase have been prepared and structurally characterized in condensed phase, e.g., {[Er(COT)$_2$)$_2$ + K]$^-$...[K(THF)$_4$]$^+$}.[38]

ESI mass spectra of mixed solutions ([K(18-c-6)][Dy(COT)$_2$], [K(18-c-6)][Y(COT)$_2$]; 0.74 mmol/L and 0.83 mmol/L, respectively) show both monomer anions as well as mixed dimers and trimers (see SI Figure 6). Interestingly, the integrated monomer intensity ratios Dy(COT)$_2^-$:Y(COT)$_2^-$ (16.5:83.5%) differ significantly from the nominal solution concentration ratio (47:53%). This may reflect either (i) the different interaction strengths of the monomer anions M(COT)$_2^-$ with the countercations [K(18-c-6)]$^+$ in solution (and the corresponding complexation equilibria) or alternatively (ii) different redox activity of the two lanthanides (leading to different rates of decomposition, e.g., by reaction with residual water, before or during ESI).

In contrast, the relative "DyDy", "DyY", and "YY" dimer intensities weighted for the respective monomer anion signals show only a slightly nonstatistical distribution (a little more [(Y(COT)$_2$)$_2$ + K]$^-$ and less [(Y(COT)$_2$)(Dy(COT)$_2$) + K]$^-$ than expected). This is an indication that dimers and higher multimer ions are generated during electrospray rather than already present in the equilibrium solution.

CID. *Monomers.* The main monomer fragmentation channel observed is reaction 1 (corresponding to roughly 30% fragmentation overall at 40 eV lab frame collision energy):

$$M(C_8H_8)_2^- \rightarrow MC_{10}H_8^- + \text{“}C_6H_8\text{”} \quad (3)$$

Figure 2 shows typical fragment mass spectra for the precursors Y(COT)$_2^-$ and Dy(COT)$_2^-$, respectively.

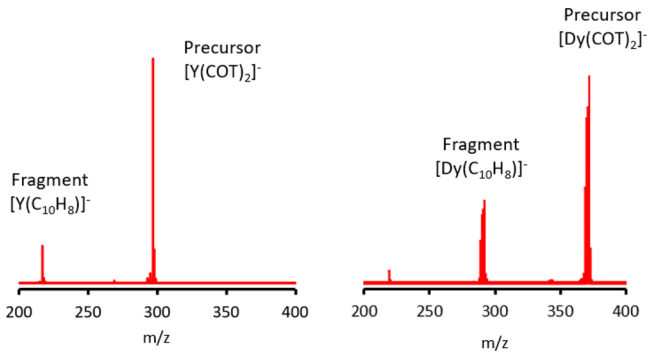

Figure 2. CID measurements for precursor Y(COT)$_2$ and Dy(COT)$_2$, respectively. Note the predominant formation of a $MC_{10}H_8$ product.

Neither the structure of the resulting $MC_{10}H_8^-$ species nor the nature of the associated neutral fragment(s) is known. In the surface science literature it has been shown that COT can be thermally decomposed on platinum surfaces (catalytically) to form benzene + acetylene.[39,40] Correspondingly, reaction 1 might in fact be yielding C_2...MCOT$^-$ + C_6H_6 + H_2 or C_2H_2...M(pentalene)$^-$ + C_6H_6 + H_2. Alternatively (and perhaps more reasonably chemically) we may be forming [$(C_5H_4)_2$M]$^-$ + 2 C_3H_4. This could be sorted out in future work with an instrument allowing detailed IMS analysis of fragment ions.

Dimers. The main dimer decay channel observed (>95% yield over the collision energy range 5−30 eV) is reaction 4:

$$[(M(COT)_2)_2 + K]^- \rightarrow KM(COT)_2 + M(COT)_2^- \quad (4)$$

or analogously for mixed dimers (M = Y and Dy), reactions 5a and 5b

$$[(Dy(COT)_2)(Y(COT)_2) + K]^- \rightarrow KDy(COT)_2 + Y(COT)_2^- \quad (5a)$$

$$\rightarrow KY(COT)_2 + Dy(COT)_2^- \quad (5b)$$

In the case of dissociation of the mixed dimer, there is a slight preference for the Dy(COT)$_2^-$ product ca. 55:45).

Next, we explore the energetics of reactions 5a and 5b using energy resolved CID measurements.

Figure 3 shows the breakdown curve of [(Dy(COT)$_2$)(Y(COT)$_2$) + K]$^-$ as well as the corresponding anion fragment yield vs lab frame collision energy. The corresponding ECE$_{50}$ value was found to be 15 eV. Note the slightly asymmetric fragmentation yield in favor of Dy(COT)$_2^-$. This is probably due simply to differing relative transmission and detection sensitivity of Dy(COT)$_2^-$ versus the significantly lighter Y(COT)$_2^-$ fragment.

IMS. *Dependence on Monomer Count.* $^{TIMS}CCS_{N2}$ were determined for all monomers and homonuclear aggregates [(M(COT)$_2$)$_{n+1}$+ nK]$^-$ (n = 0−2 and Ln = Y or Dy) (Figures

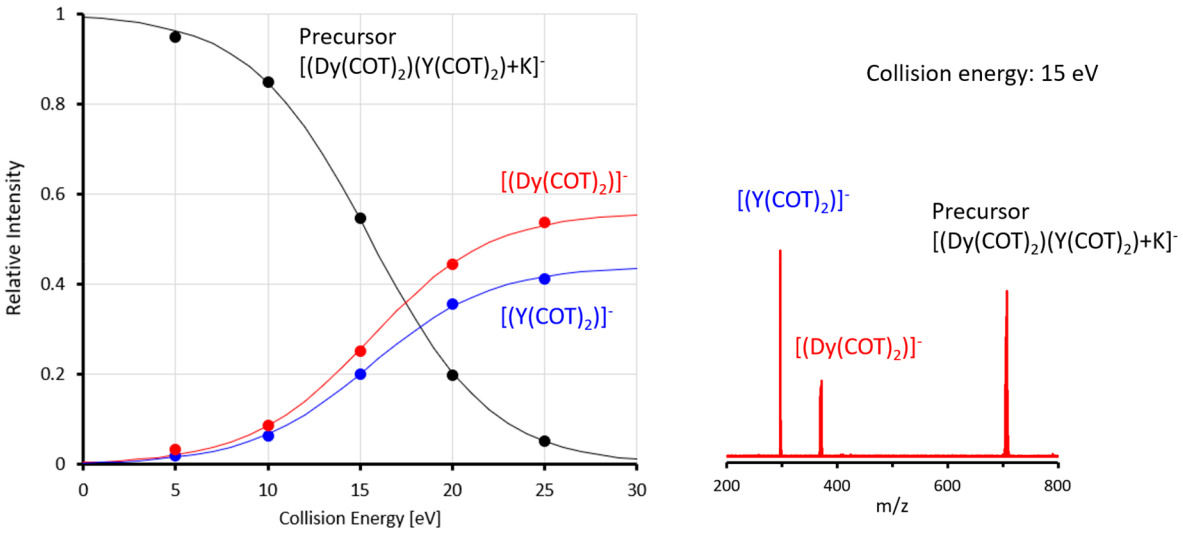

Figure 3. (Left) CID breakdown curve of $[(Dy(COT)_2)(Y(COT)_2) + K]$ together with $Dy(COT)_2$ and $Y(COT)_2$ product formation yield vs lab frame collision energy. (Right) CID mass spectrum at 15 eV lab frame collision energy.

4–6). In each case, only one peak was observed in the corresponding mobilograms with no indication of separable

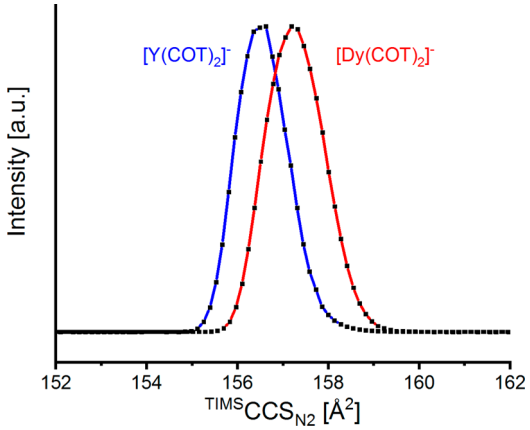

Figure 4. Mobilograms (ion intensity versus collision cross section) for $Dy(COT)_2$ and $Y(COT)_2$. Note: the clearly observable CCS increases when Dy is substituted for Y.

isomers. While $n = 3$ was clearly identified by MS in the case of Y and Dy, corresponding IMS measurements were not possible for low S/N reasons. The CCS values obtained show a roughly linear dependence on n (156.3 Å^2 ($n = 0$), 237.3 Å^2 (n =1) and

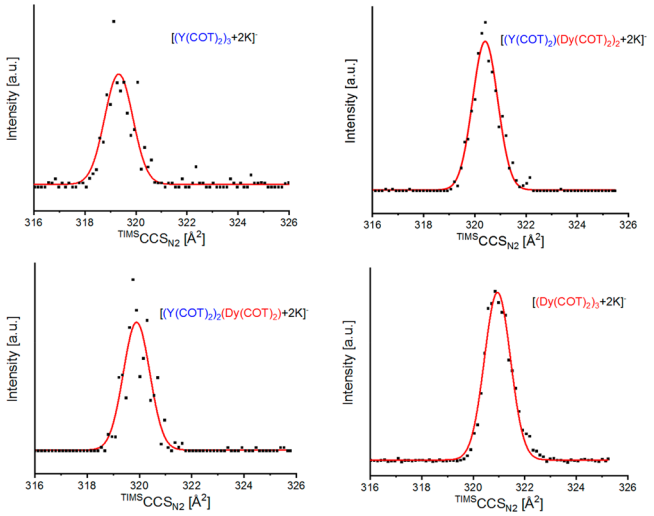

Figure 6. Mobilograms for $[(Y(COT)_2)_3 + 2K]$, $[(Y(COT)_2)_2(Dy(COT)_2) + 2K]$, $[(Y(COT)_2)(Dy(COT)_2)_2 + 2K]$, and $[(Dy(COT)_2)_3 + 2K]$.

320.1 Å^2 ($n = 2$) for Y and 157.7 Å^2 ($n = 0$), 238.4 Å^2 ($n = 1$) and 321.6 Å^2 ($n = 2$) for Dy); see also Table 1.

Dependence on Dy/Y Composition. $^{TIMS}CCS_{N2}$ was determined for all possible dimers ("Y_2", corresponding to $[(Y(COT)_2)_2 + K]^-$, "YDy" and "Dy_2") and trimers ("Y_3",

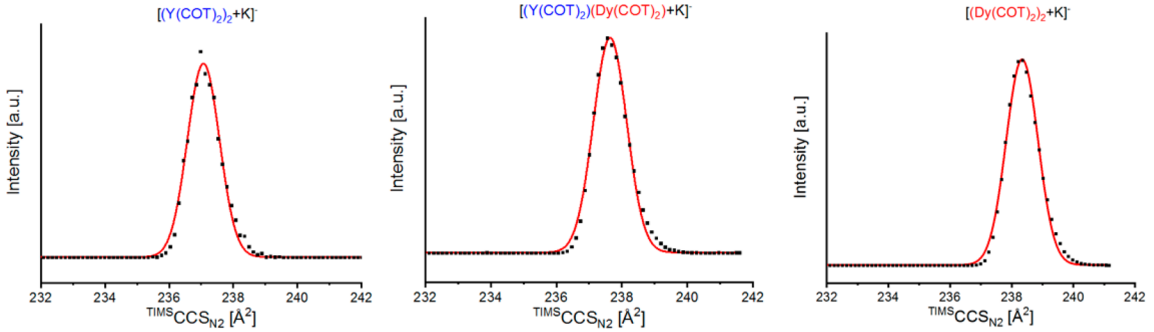

Figure 5. Mobilograms for $[(Y(COT)_2)_2 + K]$, $[(Y(COT)_2)(Dy(COT)_2) + K]$, and $[(Dy(COT)_2)_2 + K]$.

Table 1. $^{TIMS}CCS_{N2}$ Values for Y- and Dy-Containing Dimers and Trimers as well as $^{Theo}CCS_{N2}$ for Best Fitting Structural Models (Linear Stacks) from DFT + Trajectory Method Calculations for Ln = Y and Dy (See Text)

	$^{TIMS}CCS_{N2}$ (Å^2)	CCS_{N2} (Mulliken) (Å^2)	CCS_{N2} (MKS) (Å^2)	CCS_{N2} (NPA) (Å^2)	CCS_{N2} (NPA) scaled by 0.97 (Å^2)
monomers					
$\|Y\|^-$	156.3	144.4 (−7.6%)	147.9 (−5.4%)	162.9 (+3.7%)	157.2 (+0.6%)
$\|Dy\|^-$	157.7	144.5 (−8.4%)	148.3 (−6.0%)	161.4 (+2.4%)	156.6 (−0.7%)
dimers					
$\|Y\|K\|Y\|^-$	237.3	224.6 (−5.4%)	226.8 (−4.4%)	244.3 (+2.9%)	237.0 (−0.1%)
$\|Y\|K\|Dy\|^-$	238.0	228.1 (−4.2%)	228.8 (−3.9%)	244.5 (+2.7%)	237.2 (−0.4%)
$\|Dy\|K\|Dy\|^-$	238.4	224.9 (−5.7%)	228.0 (−4.4%)	243.4 (+2.1%)	236.1 (−1.0%)
trimers					
$\|Y\|K\|Y\|K\|Y\|^-$	320.1	312.1 (−2.5%)	312.8 (−2.3%)	333.7 (+4.2%)	323.7 (+1.1%)
$\|Y\|K\|Y\|K\|Dy\|^-$	320.5	313.6 (−2.1%)	314.9 (−1.8%)	334.6 (+4.4%)	324.5 (+1.3%)
$\|Y\|K\|Dy\|K\|Y\|^-$		312.5 (−2.5%)	313.4 (−2.2%)	334.0 (+4.2%)	324.0 (+1.1%)
$\|Y\|K\|Dy\|K\|Dy\|^-$	321.1	313.4 (−2.4%)	314.4 (−2.1%)	333.6 (+4.5%)	323.6 (+0.8%)
$\|Dy\|K\|Y\|K\|Dy\|^-$		315.0 (−1.9%)	316.9 (−1.3%)	335.5 (+3.9%)	325.5 (+1.4%)
$\|Dy\|K\|Dy\|K\|Dy\|^-$	321.6	313.7 (−2.4%)	315.1 (−2.0%)	332.4 (+3.3%)	322.4 (+0.2%)

"YDy_2", "Y_2Dy", and "Dy_3") accessible by electrospray of solution mixtures of ($[K^+(18\text{-c-}6)][Dy(COT)_2^-]$, $[K^+(18\text{-c-}6)][Y(COT)_2^-]$; 0.74 mmol/L and 0.83 mmol/L, respectively). The $^{TIMS}CCS_{N2}$ values are shown in Table 1. For the mixed species again no multiple isomers were resolvable. There were, however, small but systematic dependencies of $^{TIMS}CCS_{N2}$ on Y/Dy composition. Interestingly, Y-containing cluster species are always somewhat smaller than their Dy containing congeners, consistent with similar topologies but smaller ionic radius of Y^{3+} versus Dy^{3+}.

Theory. We performed DFT and TM method calculations to predict $^{TM}CCS_{N2}$ for $Dy(COT)_2^-$, $Y(COT)_2^-$, as well as several plausible isomers of K^+-linked dimers and trimers (homo- and heteronuclear). The optimized geometries and relative energies of all isomers considered are shown in Figure 7 and Figure S4. The corresponding starting structures for the monomer anions were based on the known molecular structures as determined from X-ray crystallography.[13,41]

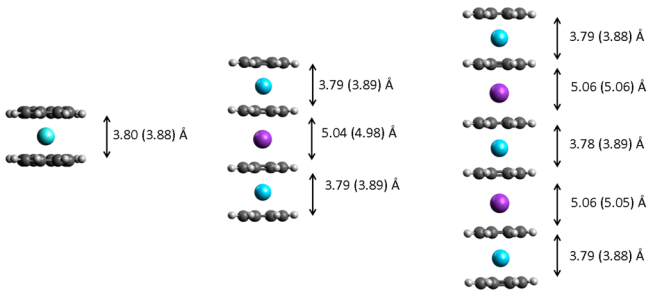

Figure 7. Overview of DFT-optimized linear stacks of $[(M(COT)_2)_{n+1} + nK]$, n = 0, 1, and 2 (yttrium: light blue, potassium: magenta). The distances refer to the COT-COT separations. Dysprosium containing complexes (numbers in brackets) have the same topologies and ca. 0.1 Å larger COT−COT distances.

In simulating $^{TM}CCS_{N2}$ for specific model structures, we used TM calculations. These incorporate element specific van der Waals parameters to model the ion-N_2 interaction. The parameters have been specifically determined by fitting for a number of light elements.[35] For dysprosium and yttrium this is not yet the case, and we therefore use the standard parameters for heavy elements implemented in IMoS ($\varepsilon = 0.42 \times 10^{-21}$ J, σ = 3.5 Å). In this study, we have performed TM simulations using the Mulliken, MKS, and NPA charge partitioning outputs of the DFT calculations. We have previously found these to provide reasonable $^{TM}CCS_{N2}$ descriptions.[18,42,43] It is interesting, that here the CCS calculated with the Mulliken and MKS-based partial charges are significantly below the experimental values, while the NPA-based partial charges result in CCS that are somewhat larger than experiment. The effect is strongest for the monomers $[Y(COT)_2]^-$ and $[Dy(COT)_2]^-$, where the methods differ by more than 10%. Using $[Y(COT)_2]^-$ as an example, we compared the average partial charges on C, H, and Y for the three methods. The Mulliken-based partial charges are very small: −0.046 on the carbon atoms, −0.01 on the hydrogens, and −0.08 on yttrium. The MKS-based partial charges are somewhat larger (in absolute terms) −0.17 on the carbon atoms, +0.074 on the hydrogens, and 0.55 on yttrium. The NPA-based partial charges are much larger (in absolute terms), −0.39 on the carbon atoms, +0.22 on the hydrogens, and 1.75 on yttrium. This large difference casts a bright light onto the ambiguity of partial charge assignment in quantum chemical calculations. Apparently the Mulliken and MKS algorithms underestimates the polarity while NPA overestimates it somewhat. If we use the monomers as calibration points (since there is no doubt about their structure) we find that NPA based $^{TM}CCS_{N2}$ are closest to the experimental values (ca. 3% above), see Table 1.

DISCUSSION

Structural Inferences by Comparing $^{TIMS}CCS_{N2}$ to $^{TM}CCS_{N2}$. For a structural characterization of the isolated ions we first compared the $^{TIMS}CCS_{N2}$ to CCS_{N2} values for various plausible DFT-based structural models for the dimer $[(Y(COT)_2{+}K)]^-$ (as shown in Figure S4). It turns out that a stack with *linearly aligned, alternating metal centers* (Figure S4a) $|Y|K|Y|^-$ (where | abbreviates COT^{2-}) provides by far the lowest relative energy (more than 0.5 eV below the next closest isomer, Figure S4b). A $|Y|Y|K|^-$ stack structure is more than 2 eV higher in energy (Figure S4e). Based on ion mobility, we cannot distinguish between the structures, since the CCS are very similar. In all cases, the Mulliken- and MKS-based values are below the experiment (237.3 Å^2) while the NPA-based value is ca. 3% above, as for the monomers. However, based on the relative energies all alternative structures can be ruled out, and in the following we therefore focus on multidecker sandwich structural motifs with linearly aligned, alternating metal centers, i.e., $|M^{3+}|K^+|M^{3+}|K^+|M^{3+}|$. Table 1 shows

$^{TIMS}CCS_{N2}$ for each of the measured $[(M(COT)_2)_{n+1}+ nK]^-$ species (n = 1 and 2, M = Dy and Y) and compares them to CCS_{N2} for the linearly aligned structural motif. The agreement between experiment and theory crucially depends on the charge partitioning algorithm. Mulliken and MKS always tend to underestimate the CCS, the effect is small for the trimers (n = 2) (ca. −2%), larger for the dimers (ca. −4%) and largest for the monomers (>−5%). On the other hand, the NPA-based values are consistently between 2.1 and 4.5% too large. This indicates that the actual charge distribution is somewhere in between that predicted by the MKS and NPA partitioning schemes. Correspondingly, if we scale the $^{TM,NPA}CCS$ values by 0.97 (using the monomers as calibration points), we can reproduce the experimental values in most cases to within 1% (see Table 1, right column).

We therefore infer that $[(M(COT)_2)_{n+1} + nK]^-$ forms multidecker sandwich structures with linearly aligned metal centers for all n probed here, similar to the structures which have previously been proposed for gas phase $Ln_n(COT)_{n+1}$ aggregates and analogous to the ferromagnetic (Eu(COT)) based nanowires with up to 1000 formula units prepared on Graphene/Ir(111) under UHV conditions by codepositing Eu and COT. In this context it is interesting to realize that according to our DFT calculations the trimer sandwich extends ca. 21.5/21.8 Å from one COT "capped" end to the other COT end (for Y/Dy, see Figure 7). The trimer comprises three $M(COT)_2^-$ units which have quite uniform COT..COT separations of 3.78−3.79/3.88−3.89 Å for Y/Dy. By contrast the two interleaved K^+ containing "spacers" have the same COT...COT separations of 5.06 Å.

As already pointed out in results above, Y-containing species (pure and mixed) have slightly smaller $^{TIMS}CCS_{N2}$ than their pure Dy congeners. This is probably related primarily to the smaller ionic radius of Y^{3+} vs Dy^{3+} and therefore smaller COT···COT separations (Y ca. 0.1 Å less than Dy).

The experimental CCS values listed in Table 1 are observed to depend roughly linearly on n. This is expected for regular cylinders (similar to the structures which we have assigned above from comparison to DFT calculations).[44] Specifically, the orientationally averaged collision cross section of a cylinder of length L and radius r in N_2 (assumed to be spherical - with r_{N2}) is given in the projection approximation by

$$\Omega = 1/2\pi(r + r_{N2})^2 + 1/2\pi(r + r_{N2})(L + r_{N2}) \quad (6)$$

Our multidecker sandwich structures to first order have constant r but n-dependent L. Approximately

$$L = (n + 1)h_{M(COT)2} + nh_{Kintercalate} \quad (7)$$

If we assume that $h_{M(COT)2} = h_{Kintercalate} = h$ the latter can be further simplified to

$$L = (2n + 1)h \quad (8)$$

And if we completely neglect the radius of the (much smaller) N_2 we obtain

$$\Omega = 1/2\pi r^2 + 1/2\pi rh(2n + 1) \quad (9)$$

based on our DFT structures and to first order: $h = 2r$. Therefore: $\Omega = 1/2\ \pi r^2 + \pi r^2(2n+1) = \pi r^2(2n+3/2)$, i.e., the near-linear trend we find in our experiment.

Two points about our DFT calculations of linear stacks and their $M(COT)_2^-$ building blocks are noteworthy in closing: (i) for the $Y(COT)_2^-$ system we explored the relative stabilities of D_{8h} (eclipsed COT rings), D_{4d} (staggered COT rings), and C_1 (fully optimized) forms. They differ by <0.05 eV, i.e., the parallel COT rings would be expected to freely rotate relative to each other at the vibrational temperatures accessed here (ca. 300 K); (ii) linear stacks beg the question of how much energy would be required for appreciable "rod" bending. In Figure S5a we plot DFT-derived relative energies for $[(Y(COT)_2)_3 + 2K]^-$ against the Y···Y···Y$^-$ angle. Bending by up to 20°, essentially about the K^+ center "hinges" (while the Y interlinked COT rings remain essentially parallel), requires only about 0.03 eV. Beyond 20° though, the energy "cost" begins to rise parabolically with further bending, as the steric interaction between K^+ interlinked COT rings becomes more appreciable. The $[(Y(COT)_2)_3+ 2K]^-$ rod behaves analogously but appears to be slightly stiffer; see Figure S5b.

Dimer Binding Energies from CID Measurements and DFT Calculations. Table 2 shows predicted stabilities for the stacked sandwich forms of all dimer (n = 1) and trimer (n = 2) combinations of $[(M(COT)_2)_{n+1}+ nK]^-$, M = Y, Dy, referenced to the infinitely separated ions (n + 1 $M(COT)_2^-$ + nK^+). Within each n, there are only minor, composition-dependent differences in stability. Overall, stability increases linearly with n indicating that additive two-body Coulomb interactions mediated by the K^+ ions are dominant. The minor composition dependent variations (of at most ca. 0.2 eV, i.e., 2% in overall stability) may result from incomplete shielding of through-ring $K^+|M^{3+}$ Coulomb repulsion by the aromatic COT^{2-} π-electrons.

Table 2. DFT-Predicted Stabilities (i.e., Differences of DFT Energies at 0 K, Zero-Point Energies Not Included) for the Stacked Sandwich Forms of All Dimers (n = 1) and Trimer (n = 2) Combinations of $[(M(COT)_2)_{n+1} + nK]^-$, M = Y, Dy[a]

dimers		trimers	
|Y|K|Y|$^-$	−6.62 eV	|Y|K|Y|K|Y|$^-$	−12.93 eV
|Y|K|Dy|$^-$	−6.66 eV	|Y|K|Y|K|Dy|$^-$	−12.97 eV
|Dy|K|Dy|$^-$	−6.73 eV	|Y|K|Dy|K|Y|$^-$	−12.95 eV
		|Y|K|Dy|K|Dy|$^-$	−13.06 eV
		|Dy|K|Y|K|Dy|$^-$	−13.01 eV
		|Dy|K|Dy|K|Dy|$^-$	−13.14 eV

[a] "Dimer" stability refers to the reaction $M^1(COT)_2 + M^2(COT)_2 + K^+ \rightarrow [M^1(COT)_2M^2(COT)_2 + K]$, whereas "trimer" stability refers to the reaction $M^1(COT)_2 + M^2(COT)_2 + M^3(COT)_2 + 2K^+ \rightarrow [M^1(COT)_2M^2(COT)_2M^3(COT)_2 + 2K]$ with M^1, M^2, M^3 = Dy, Y.

It would be interesting to compare predicted binding energies to our CID measurements for $[(Dy(COT)_2)(Y(COT)_2) + K]^-$. Based on the DFT calculations for M = Y, Dy, we expect dissociation energies of 1.85 and 1.81 eV for reactions 5a and 5b, respectively. Unfortunately, energy-resolved CID measurements of lanthanide complexes and their aggregates are still quite rare. Consequently, thermometer ion scales with which to calibrate breakdown curves have yet to be developed. Our linear stacks held together mainly by additive Coulombic interactions may be useful in this regard.

Concerning the reason for the slight preference of reaction 5b in the fragmentation of $[Dy(COT)_2^-...K^+...Y(COT)_2^-]^-$, we can only speculate as the calculated energy differences (1.85 eV vs 1.81 eV) are within the uncertainty of the method.

CONCLUSIONS

Electrospray ionization of THF solutions of preformed $[K(18\text{-}c\text{-}6)][M(COT)_2]$ (where $M(COT)_2^-$ corresponds to M(III) = Y(III) and Dy(III) stabilized by two planar cyclooctatetraene dianion ligands (COT^{2-}) and $K(18\text{-}c\text{-}6)^+$ is the counterion comprising K^+ complexed with a crown ether ($C_{12}H_{24}O_6$)) yields $[(M(COT)_2)_{n+1} + nK]^-$ with n = 0−3. High resolution trapped ion mobility spectrometry (TIMS) in combination with density functional theory calculations shows that the aggregates with n = 1 and 2 (3 was not measurable by TIMS) form multidecker stacks interlinked by potassium cations. The alternating metal ions are aligned linearly: COT^{2-}−M^{3+}−COT^{2-}−K^+−COT^{2-}−M^{3+}−COT^{2-}. Different M(III) ionic radii lead to slight but well-resolvable changes in the overall heights of the multidecker stacks. CID measurements indicate that the aggregates fragment by cleavage at the K^+ interconnect.

A number of issues remain open for future studies:

(a) What are the dominant molecular entities present in solution? For example, does a $K^+...M(COT)_2^-$ or $K^+(18\text{-}c\text{-}6)]\cdots[M(COT)_2^-$ contact ion pair exist in a room temperature THF solution or is the cation/anion complex separated by one or more solvent molecules? Under our conditions, the anion mass spectra do not show any adducts with 18-crown-6 even though the starting material was $[K^+(18\text{-}c\text{-}6)][M(COT)_2^-]$. On the other hand, X-ray crystallography of $[K(18\text{-}c\text{-}6)(THF)_2][Er(COT)_2]$, i.e., of a crystal obtained from THF solutions in excess of $K(18\text{-}c\text{-}6)^+$, shows two THF solvent molecules attached to each crown.[12] Solvent molecules therefore appear to be important in stabilizing $K^+(18\text{-}c\text{-}6)$ and possibly also in mediating its interaction with $M(COT)_2^-$. Our results suggest that during ESI and without such solvent stabilization, some K^+ detaches from the 18-crown-6 and attaches to the $M(COT)_2^-$ moiety. In this context it is interesting to note that DFT (TPSS, def2SVP) finds a $K^+...18\text{-}c\text{-}6$ interaction strength of ca. 3.2 eV versus 4.8 eV for $K^+...M(COT)_2^-$; i.e., the K^+ transfer would be exoergic by ca. 1.6 eV.

(b) Can larger $[(M(COT)_2)_{n+1} + nK]^-$ stacks be prepared by appropriate tuning of ESI source conditions and if so do their structures remain linear? Based on analogous DFT calculations for larger linear stacks, we would for example expect n = 3, 4 to have a collision cross section of 412 and 504 Å^2 and an overall height of 30.3 Å and 39.2 Å, respectively.

(c) Can other countercations be inserted between the $M(COT)_2^-$ units, e.g., larger or smaller alkali ions stabilized in the condensed phase synthesis by larger or smaller crown ethers? These would presumably allow some first order tuning of M(III)···M(III) separations and therefore also couplings.

(d) Apart from ferromagnetic coupling already alluded to in the introduction (though at generally smaller M···M separations than accessible in the present aggregates) there is also the possibility that the photoluminescence of individual $M(COT)_2^-$ units may be measurably influenced by (excitation of) neighboring units in the stack. This could be explored in future low temperature ion trapping experiments. In this context it is interesting to note that the interesting photoluminescence of $M(COT)_2^-$ derived materials is only beginning to be explored.[45,46] There is reason to expect that COT^{2-} has a long-lived triplet state in the visible and could thus be used to sensitize Ln(III) emission.[47,48]

ASSOCIATED CONTENT

Supporting Information

The Supporting Information is available free of charge at https://pubs.acs.org/doi/10.1021/jasms.1c00378.

NMR data, plot of DFT-derived structures, relative binding energy vs bond angle, mass spectrum of mixture (PDF)

DFT-optimized structures *xyz*-files (ZIP)

AUTHOR INFORMATION

Corresponding Author

Manfred M. Kappes − *Institute of Physical Chemistry, Karlsruhe Institute of Technology (KIT), 76131 Karlsruhe, Germany; Institute of Nanotechnology, Karlsruhe Institute of Technology (KIT), 76344 Eggenstein-Leopoldshafen, Germany;* orcid.org/0000-0002-1199-1730; Email: manfred.kappes@kit.edu

Authors

Erik K. Schneider − *Institute of Physical Chemistry, Karlsruhe Institute of Technology (KIT), 76131 Karlsruhe, Germany*

Patrick Weis − *Institute of Physical Chemistry, Karlsruhe Institute of Technology (KIT), 76131 Karlsruhe, Germany;* orcid.org/0000-0001-7006-6759

Luca Münzfeld − *Institute of Inorganic Chemistry, Karlsruhe Institute of Technology (KIT), 76131 Karlsruhe, Germany*

Peter W. Roesky − *Institute of Inorganic Chemistry, Karlsruhe Institute of Technology (KIT), 76131 Karlsruhe, Germany*

Complete contact information is available at: https://pubs.acs.org/10.1021/jasms.1c00378

Notes

The authors declare no competing financial interest.

ACKNOWLEDGMENTS

M.K., P.R., and P.W. gratefully acknowledge financial support from the DFG-funded transregional collaborative research center SFB/TRR 88 “Cooperative Effects in Homo and Heterometallic Complexes (3MET)” (projects B3, C3, and C6) which helped initiate this study.

REFERENCES

(1) Hayes, R. G.; Thomas, J. L. Synthesis of Cyclooctatetraenyleuropium and Cyclooctatetraenylytterbium. *J. Am. Chem. Soc.* **1969**, *91*, 6876.

(2) Mares, F.; Hodgson, K.; Streitwieser, A., Jr, Lanthanide Complexes with Cyclooctatetraene Di-Anion. *J. Organomet. Chem.* **1970**, *24*.C68

(3) Weis, P.; Kemper, P. R.; Bowers, M. T. Structures and Energetics of V-N(C6H6)(M)(+) Clusters: Evidence for a Quintuple-Decker Sandwich. *J. Phys. Chem. A* **1997**, *101*, 8207−8213.

(4) Hoshino, K.; Kurikawa, T.; Takeda, H.; Nakajima, A.; Kaya, K. Structures and Ionization Energies of Sandwich Clusters (V-N(Benzene)(M)). *J. Phys. Chem.* **1995**, *99*, 3053−3055.

(5) Kurikawa, T.; Negishi, Y.; Hayakawa, F.; Nagao, S.; Miyajima, K.; Nakajima, A.; Kaya, K. Multiple-Decker Sandwich Complexes of Lanthanide− 1, 3, 5, 7-Cyclooctatetraene [Ln N (C8H8) M](Ln= Ce, Nd, Eu, Ho, and Yb); Localized Ionic Bonding Structure. *J. Am. Chem. Soc.* **1998**, *120*, 11766−11772.

(6) Hosoya, N.; Takegami, R.; Suzumura, J.; Yada, K.; Koyasu, K.; Miyajima, K.; Mitsui, M.; Knickelbein, M. B.; Yabushita, S.; Nakajima, A. Lanthanide Organometallic Sandwich Nanowires: Formation Mechanism. *J. Phys. Chem. A* **2005**, *109*, 9−12.

(7) Miyajima, K.; Knickelbein, M.; Nakajima, A. Stern-Gerlach Studies of Organometallic Sandwich Clusters. *Eur. Phys. J. D* **2005**, *34*, 177−182.
(8) Huttmann, F.; Rothenbach, N.; Kraus, S.; Ollefs, K.; Arruda, L. M.; Bernien, M.; Thonig, D.; Delin, A.; Fransson, J.; Kummer, K. Europium Cyclooctatetraene Nanowire Carpets: A Low-Dimensional, Organometallic, and Ferromagnetic Insulator. *J. Phys. Chem. Lett.* **2019**, *10*, 911−917.
(9) Hosoya, N.; Yada, K.; Masuda, T.; Nakajo, E.; Yabushita, S.; Nakajima, A. Investigation of the Electronic Structures of Organolanthanide Sandwich Complex Anions by Photoelectron Spectroscopy: 4f Orbital Contribution in the Metal−Ligand Interaction. *J. Phys. Chem. A* **2014**, *118*, 3051−3060.
(10) Kurikawa, T.; Negishi, Y.; Hayakawa, F.; Nagao, S.; Miyajima, K.; Nakajima, A.; Kaya, K. Generation and Electronic Properties of Lanthanide-Cyclooctatetraene Organometallic Clusters in Gas Phase. *Eur. Phys. J. D* **1999**, *9*, 283−287.
(11) Nakajo, E.; Masuda, T.; Yabushita, S. Theoretical Study on the Photoelectron Spectra of Ln(COT)(2)(−): Lanthanide Dependence of the Metal-Ligand Interaction. *J. Phys. Chem. A* **2016**, *120*, 9529−9544.
(12) Meihaus, K. R.; Long, J. R. Magnetic Blocking at 10 K and a Dipolar-Mediated Avalanche in Salts of the Bis(H^8-Cyclooctatetraenide) Complex $[Er(COT)_2]^-$. *J. Am. Chem. Soc.* **2013**, *135*, 17952−17957.
(13) Hodgson, K. O.; Mares, F.; Starks, D. F.; Streitwieser, A. Lanthanide(III) Complexes with Cyclooctatetraene Dianion - Synthetic Chemistry, Characterization, and Physical-Properties. *J. Am. Chem. Soc.* **1973**, *95*, 8650−8658.
(14) Katz, T. J. The Cycloöctatetraenyl Dianion. *J. Am. Chem. Soc.* **1960**, *82*, 3784−3785.
(15) Michelmann, K.; Silveira, J. A.; Ridgeway, M. E.; Park, M. A. Fundamentals of Trapped Ion Mobility Spectrometry. *J. Am. Soc. Mass Spectrom.* **2015**, *26*, 14−24.
(16) Revercomb, H.; Mason, E. A. Theory of Plasma Chromatography/Gaseous Electrophoresis. Review. *Anal. Chem.* **1975**, *47*, 970−983.
(17) Stow, S. M.; Causon, T. J.; Zheng, X.; Kurulugama, R. T.; Mairinger, T.; May, J. C.; Rennie, E. E.; Baker, E. S.; Smith, R. D.; McLean, J. A. An Interlaboratory Evaluation of Drift Tube Ion Mobility−Mass Spectrometry Collision Cross Section Measurements. *Anal. Chem.* **2017**, *89*, 9048−9055.
(18) Weis, P.; Hennrich, F.; Fischer, R.; Schneider, E. K.; Neumaier, M.; Kappes, M. M. Probing the Structure of Giant Fullerenes by High Resolution Trapped Ion Mobility Spectrometry. *Phys. Chem. Chem. Phys.* **2019**, *21*, 18877−18892.
(19) Hennrich, F.; Schneider, E.; Weis, P.; Kappes, M. M. Comparing Empty and Filled Fullerene Cages with High-Resolution Trapped Ion Mobility Spectrometry. *J. Am. Soc. Mass Spectrom.* **2019**, *30*, 1973−1980.
(20) *Turbomole V7.5.1 2021, a Development of University of Karlsruhe and Forschungszentrum Karlsruhe Gmbh, 1989−2007*, Turbomole Gmbh, since 2007. Available from https://www.turbomole.org.
(21) Perdew, J. P.; Wang, Y. Accurate and Simple Analytic Representation of the Electron-Gas Correlation Energy. *Phys. Rev. B* **1992**, *45*, 13244.
(22) Perdew, J. P.; Wang, Y. Erratum: Accurate and Simple Analytic Representation of the Electron-Gas Correlation Energy [Phys. Rev. B 45, 13244 (1992)]. *Phys. Rev. B* **2018**, *98*, 079904.
(23) Tao, J.; Perdew, J. P.; Staroverov, V. N.; Scuseria, G. E. Climbing the Density Functional Ladder: Nonempirical Meta−Generalized Gradient Approximation Designed for Molecules and Solids. *Phys. Rev. Lett.* **2003**, *91*, 146401.
(24) Eichkorn, K.; Treutler, O.; Öhm, H.; Häser, M.; Ahlrichs, R. Auxiliary Basis Sets to Approximate Coulomb Potentials. *Chem. Phys. Lett.* **1995**, *240*, 283−290.
(25) Schäfer, A.; Horn, H.; Ahlrichs, R. Fully Optimized Contracted Gaussian Basis Sets for Atoms Li to Kr. *J. Chem. Phys.* **1992**, *97*, 2571−2577.
(26) Weigend, F. Accurate Coulomb-Fitting Basis Sets for H to Rn. *Phys. Chem. Chem. Phys.* **2006**, *8*, 1057−1065.
(27) Weigend, F.; Ahlrichs, R. Balanced Basis Sets of Split Valence, Triple Zeta Valence and Quadruple Zeta Valence Quality for H to Rn: Design and Assessment of Accuracy. *Phys. Chem. Chem. Phys.* **2005**, *7*, 3297−3305.
(28) Weigend, F.; Häser, M.; Patzelt, H.; Ahlrichs, R. Ri-Mp2: Optimized Auxiliary Basis Sets and Demonstration of Efficiency. *Chem. Phys. Lett.* **1998**, *294*, 143−152.
(29) Eichkorn, K.; Weigend, F.; Treutler, O.; Ahlrichs, R. Auxiliary Basis Sets for Main Row Atoms and Transition Metals and Their Use to Approximate Coulomb Potentials. *Theor. Chem. Acc.* **1997**, *97*, 119−124.
(30) Sierka, M.; Hogekamp, A.; Ahlrichs, R. Fast Evaluation of the Coulomb Potential for Electron Densities Using Multipole Accelerated Resolution of Identity Approximation. *J. Chem. Phys.* **2003**, *118*, 9136−9148.
(31) Grimme, S.; Antony, J.; Ehrlich, S.; Krieg, H. A Consistent and Accurate Ab Initio Parametrization of Density Functional Dispersion Correction (DFT-D) for the 94 Elements H-Pu. *J. Chem. Phys.* **2010**, *132*, 154104.
(32) Grimmel, S.; Schoendorff, G.; Wilson, A. K. Gauging the Performance of Density Functionals for Lanthanide-Containing Molecules. *J. Chem. Theory Comput.* **2016**, *12*, 1259−1266.
(33) Wiberg, N. *Lehrbuch Der Anorganischen Chemie*; De Gruyter, 2008; p 1973.
(34) Larriba, C.; Hogan, C. J. Ion Mobilities in Diatomic Gases: Measurement Versus Prediction with Non-Specular Scattering Models. *J. Phys. Chem. A* **2013**, *117*, 3887−3901.
(35) Wu, T. Y.; Derrick, J.; Nahin, M.; Chen, X.; Larriba-Andaluz, C. Optimization of Long Range Potential Interaction Parameters in Ion Mobility Spectrometry. *J. Chem. Phys.* **2018**, *148*, 074102.
(36) Singh, U. C.; Kollman, P. A. An Approach to Computing Electrostatic Charges for Molecules. *J. Comput. Chem.* **1984**, *5*, 129−145.
(37) Reed, A. E.; Weinstock, R. B.; Weinhold, F. Natural-Population Analysis. *J. Chem. Phys.* **1985**, *83*, 735−746.
(38) Xia, J. S.; Jin, Z. S.; Chen, W. Q. Synthesis and Crystal-Structure of a New Lanthanide Cyclooctatetraene Complex (Eta-8-C8H8)Er(Mu-Eta-8-C8H8)K(Mu-Eta-8-C8H8)Er(Mu-Eta-8-C8H8)K(THF)4. *J. Chem. Soc.-Chem. Commun.* **1991**, 1214−1215.
(39) Hostetler, M. J.; Nuzzo, R. G.; Girolami, G. S.; Dubois, L. H. Structure-Reactivity Correlations in the Reactions of Hydrocarbons on Transition-Metal Surfaces. 1. Ring Contraction of Cyclooctene, 1,3-Cyclooctadiene, 1,5-Cyclooctadiene, and Cyclooctatetraene to Benzene on a Platinum(111) Surface. *J. Phys. Chem.* **1994**, *98*, 2952−2962.
(40) Hostetler, M. J.; Dubois, L. H.; Nuzzo, R. G.; Girolami, G. S. Ring Contraction of Cyclooctene, 1,3-Cyclooctadiene, 1,5-Cyclooctadiene, and Cyclooctatetraene to Benzene on Platinum(111) Surfaces. *J. Am. Chem. Soc.* **1993**, *115*, 2044−2046.
(41) Meihaus, K. R.; Long, J. R. Magnetic Blocking at 10 K and a Dipolar-Mediated Avalanche in Salts of the Bis(Eta(8)-Cyclooctatetraenide) Complex Er(COT)(2) (−). *J. Am. Chem. Soc.* **2013**, *135*, 17952−17957.
(42) Baksi, A.; Schneider, E. K.; Weis, P.; Chakraborty, I.; Fuhr, O.; Lebedkin, S.; Parak, W. J.; Kappes, M. M. Linear Size Contraction of Ligand Protected Ag-29 Clusters by Substituting Ag with Cu. *ACS Nano* **2020**, *14*, 15064−15070.
(43) Zagorec-Marks, W.; Dodson, L. G.; Weis, P.; Schneider, E. K.; Kappes, M. M.; Weber, J. M. Intrinsic Structure and Electronic Spectrum of Deprotonated Biliverdin: Cryogenic Ion Spectroscopy and Ion Mobility. *J. Am. Chem. Soc.* **2021**, *143*, 17778−17785.
(44) Jarrold, M. F.; Constant, V. A. Silicon Cluster Ions - Evidence for a Structural Transition. *Phys. Rev. Lett.* **1991**, *67*, 2994−2997.
(45) Tsuji, T.; Hosoya, N.; Fukazawa, S.; Sugiyama, R.; Iwasa, T.; Tsunoyama, H.; Hamaki, H.; Tokitoh, N.; Nakajima, A. Liquid-Phase Synthesis of Multidecker Organoeuropium Sandwich Complexes and Their Physical Properties. *J. Phys. Chem. C* **2014**, *118*, 5896−5907.

(46) Kawasaki, K.; Sugiyama, R.; Tsuji, T.; Iwasa, T.; Tsunoyama, H.; Mizuhata, Y.; Tokitoh, N.; Nakajima, A. A Designer Ligand Field for Blue-Green Luminescence of Organoeuropium(II) Sandwich Complexes with Cyclononatetraenyl Ligands. *Chem. Commun.* **2017**, *53*, 6557−6560.
(47) Dvorak, V.; Michl, J. Photoionization of Anions in Rigid Media - Absorption and Emission-Spectroscopy of Cyclooctatetraene Radical-Anion, Its Ion-Pairs, and Triple Ions. *J. Am. Chem. Soc.* **1976**, *98*, 1080−1086.
(48) Lebedkin, S. Private communication.